Anisotropic electrical conductivity of oxygen-deficient tungsten oxide films with epitaxially stabilized 1D atomic defect tunnels

Gowoon Kim,* Bin Feng, Sangkyun Ryu, Hai Jun Cho, Hyoungjeen Jeen, Yuichi Ikuhara, and Hiromichi Ohta*

ABSTRACT

Materials having an anisotropic crystal structure often exhibit anisotropy in the electrical conductivity. Compared to complex transition metal oxides (TMOs), simple TMOs rarely show large anisotropic electrical conductivity due to their simple crystal structure. Here we focus on the anisotropy in the electrical conductivity of simple TMO, oxygen-deficient tungsten oxide (WO_x) with an anisotropic crystal structure. We fabricated several WO_x films by pulsed laser deposition technique on lattice matched (110)-oriented $LaAlO_3$ substrate under controlled oxygen atmosphere. The crystallographic analyses of the WO_x films revealed that highly dense atomic defect tunnels were aligned one dimensionally (1D) along [001] $LaAlO_3$. The electrical conductivity along the 1D atomic defect tunnels was ~5 times larger than that across the tunnels. The present approach, introduction of 1D atomic defect tunnels might be useful to design simple TMOs exhibiting anisotropic electrical conductivity.

INTRODUCTION

Materials having an anisotropic crystal structure often exhibit anisotropy in the electrical conductivity.[1-9] Since there are wide varieties of crystal structures in complex transition metal oxides (TMOs), many complex TMOs exhibit anisotropy in the electrical conductivity as summarized in **Table S1**.[10-15] For example, the electrical conductivity of hollandite $BaRu_6O_{12}$ along double chain of edged sharing RuO_6 is ~6 times larger than the perpendicular direction at 300K.[16] In the case of perovskite layered structure $YBa_2Cu_3O_y$ ($6.6 \leq y \leq 7$), the in-plane electrical conductivity along the CuO chain has 1.2~2.7 times larger than across CuO chain direction.[15] However, simple TMO that exhibits anisotropy in the electrical conductivity is rare due to their simple crystal structure. One exception is NbO_2.[17] Since the overlap integral of 4d orbitals, which is major component of the conduction band, in NbO_2 is relatively small, the electrical conductivity decreases when the bond angle of Nb−O−Nb is distorted from 180°. On the other hand, the overlap integral of widely spread 5d orbitals in TMOs is large, therefore, the electrical conductivity is less sensitive to the bond angle of TM−O−TM. Hence, it is difficult to find simple 5d TMOs that exhibit anisotropy in the electrical conductivity.

Among many simple 5d TMOs, we focus on oxygen-deficient tungsten oxide (WO_x) with an anisotropic crystal structure (**Figure 1a**, unit cell).[18] There are one dimensional (1D) vacancy channels in the WO_x crystal (**Figure 1b**), which we defined as the 1D atomic defect tunnels (yellow ring). We expected there is a large anisotropy in the electrical conductivity along/across the tunnels. In order to clarify the anisotropy in the electrical conductivity of WO_x, large-size single crystals or epitaxial films are required. We assumed that WO_x film

with aligned atomic defect tunnel structure can be grown on lattice matched (110)-oriented LaAlO$_3$ single crystal substrate. Although there is almost no similarity of the atomic arrangement between WO$_x$ along the b-axis and LaAlO$_3$ along [001], the distance between two neighboring oxygens in WO$_x$ along the c-axis and LaAlO$_3$ along [1$\bar{1}$0] is the same (0.379 nm). Previous studies reveal that the oxygen content x in WO$_x$ can be controlled by modulating the oxygen pressure during the WO$_x$ film deposition by pulsed laser deposition technique.[19] We focused on oxygen deficient WO$_x$ from these points of view.

Here we show that oxygen-deficient WO$_x$ epitaxial films with 1D atomic defect tunnels exhibit large anisotropy of the electrical conductivity. We fabricated several WO$_x$ films with highly dense atomic defect tunnels, which were aligned one dimensionally along [001] LaAlO$_3$ by pulsed laser deposition technique. The electrical conductivity along the 1D atomic defect tunnels was ~5 times larger than that across the tunnels. The present approach, introduction of 1D atomic defect tunnels might be useful to design simple TMOs exhibiting anisotropic electrical conductivity.

RESULTS AND DISCUSSION

We fabricated oxygen-deficient WO$_x$ films on (110)-oriented LaAlO$_3$ single crystal substrates by pulsed laser deposition (PLD) technique. The oxygen pressure was precisely controlled (4 − 8.3 Pa) during the PLD to modulate the oxygen content x in WO$_x$. After the film growth, we measured the oxygen content x in the WO$_x$ films by measuring the X-ray

photoelectron spectroscopy (XPS) spectra (**Figure S1**). By analyzing the peak area ratio of W, the x in the WO_x films was modulated from 2.778 to 3 (**Figure S2**).

Figure 2a shows out-of-plane X-ray diffraction (XRD) pattern of the WO_x films around the (110) diffraction peak of the $LaAlO_3$ substrate. When $x = 3$, an intense diffraction peak of 110 WO_3 (assuming ReO_3 structure) is observed at $q_z/2\pi = 3.8$ nm^{-1} together with Pendellösung fringes (|), indicating a strong (110) orientation of the film. The peak intensity decreases and the peak position shits to the lower $q_z/2\pi$ side with decreasing x, indicating that the orientation of WO_x crystal becomes weak and the lattice expansion occurs with decreasing x as shown in **Figure 2b**. Since the ionic radius of W^{5+} (0.62 Å) is larger than that of W^{6+} (0.60 Å), the lattice expansion occurred by the removal of oxygen from ReO_3-type WO_3 lattice. Then, we observed the surface morphologies of the WO_3 (**Figure 2c**) and $WO_{2.778}$ (**Figure 2d**) films by atomic force microscopy (AFM). The WO_3 film surface is smooth that composed of tiny grains and featureless whereas the $WO_{2.778}$ surface is an anisotropic structure that composed of long rectangular shaped grains (L ~600 nm, W ~20 nm) aligned along [001]. The reflection high-energy electron diffraction (RHEED) patterns of the WO_3 (**Figure 2e**) and $WO_{2.778}$ (**Figure 2f**) films clearly indicate the structural difference; Intense streak RHEED patterns were observed in **Figure 2e**, indicating that the strong orientation and the smooth surface of the WO_3 film. On the other hand, intense streak RHEED pattern was observed in **Figure 2f** azimuth [1$\bar{1}$0] and halo-like RHEED pattern was

observed azimuth [001]. This clearly indicates that there is a 1D lattice along [001] whereas the atomic arrangement along [1$\bar{1}$0] is almost random.

To further clarify the anisotropic structure, we measured X-ray reciprocal space mappings (RSMs) around the Bragg diffraction spots of 22$\bar{2}$ LaAlO$_3$ and 310 LaAlO$_3$. An intense diffraction spot of 44$\bar{4}$ WO$_3$ was observed together with 22$\bar{2}$ LaAlO$_3$ when azimuth is [001] (**Figure S3a**) and two intense diffraction spots of 620 and 230 WO$_3$ were observed together with 310 LaAlO$_3$ when azimuth was [1$\bar{1}$0] (**Figure S4a**). An intense spot of WO$_{2.778}$ was observed together with 22$\bar{2}$ LaAlO$_3$ spot when azimuth was [001] (**Figure S3b**). Weak tail in the q_z direction was also observed. On the other hand, a very broad streak of WO$_{2.778}$ was observed together with 310 LaAlO$_3$ when azimuth was [1$\bar{1}$0] (**Figure S4b**), indicating that the lateral coherence length along [1$\bar{1}$0] was extremely short. It should be noted that the in-plane peak position ($q_{[001]}/2\pi$) of the WO$_3$ and WO$_{2.778}$ peaks was same with that of LaAlO$_3$, indicating coherent epitaxial growth occurred in all cases. From these results, we judged that almost uniaxially oriented oxygen deficient WO$_x$ films along [001] were successfully fabricated on (110) LaAlO$_3$ substrate.

In order to visualize the atomic arrangement of oxygen-deficient WO$_x$, we performed the cross-sectional high-angle annular dark-field (HAADF) scanning transmission electron microscopy (STEM) observations (**Figure 3**) of the WO$_{2.778}$ film. Rather disordered atomic columns were observed along [001] (**Figures 3a and 3c**) together with many dot-like dark

contrast whereas ordered stripes were observed along [1$\bar{1}$0] (**Figures 3b and 3d**). The diameter of the dot-like contrast was ~0.3 nm. The dot-like contrast was randomly distributed in surrounding random atomic column. These results clearly indicate that high density atomic defect tunnels were successfully stabilized one dimensionally in the $WO_{2.778}$ film. It should be noted that the energy-dispersive X-ray spectroscopy (EDS) mappings around the interface between the film and the substrate indicated that any chemical reaction occurred at the interface (**Figure S5**). Although the detailed crystal growth of the $WO_{2.778}$ film is still unclear yet, we imagine as following. Since the oxygen sublattices of the $WO_{2.778}$ and (110) $LaAlO_3$ are matched well along [001] whereas there is no lattice matching along [1$\bar{1}$0], uniaxially orientated crystal growth occurred. During the film growth, atomic arrangement moved and the 1D atomic defect tunnels were formed to minimize the energy.

Then, we measured the electrical conductivity of the resultant WO_x films along the [001] and [1$\bar{1}$0]. **Figure 4a** shows the electrical conductivity (σ) measured by dc four-probe method at room temperature. The σ increased from ~0.4 to ~5 S cm^{-1} with decreasing x from 2.987 to 2.960 in both directions. The electron configuration of W^{5+} is $5d^1$ and the d-electron plays as the carrier electron. Therefore, the σ increased with decreasing x. When $x < 2.96$, the σ along [001] was always higher than that along [1$\bar{1}$0], indicating the anisotropy of the electrical conductivity. The anisotropy increased with decreasing x. When $x = 2.778$, the σ along [001] was 1700 S cm^{-1} whereas that along [1$\bar{1}$0] was 360 S cm^{-1}, indicating anisotropy of σ ~5. In order to clarify the origin of the anisotropy of σ, we measured the thermopower (S) (**Figure**

4b). The absolute values of S decreased from ~360 to ~20 μV K^{-1} with decreasing x, independently on the directions. This indicates that the carrier concentration increased with decreasing x and there is no anisotropy in the carrier concentration. Then, we plotted the S as a function of log-scaled σ (Jonker plot) of $x = 2.778$, 2.82 and 2.853 (**Figure 4b inset**), which reveals that the carrier mobility along [001] is higher than that along [1$\bar{1}$0].

Next, we measured the $\sigma-T$ curves (**Figure S6a**). The σ along [001] is always higher than that along [1$\bar{1}$0]. The σ increased with increasing temperature in all cases. Then, we extracted the activation energy (E_a) of the σ around room temperature. **Figure S6b** shows E_a as a function of x in WO$_x$. The E_a decreased with decreasing x. When $x < 2.96$, the E_a along [001] is clearly smaller than that along [1$\bar{1}$0]. Since there is no anisotropy in the carrier concentration, the difference in the E_a reflects the anisotropy in carrier mobility. There are two possible origins of the difference in the carrier mobility (μ). One is the difference in the carrier relaxation time (τ) and the other one is the difference in the carrier effective mass (m^*), because μ is expressed as $\mu = e \cdot \tau \cdot m^{*-1}$, where e is electron charge.

In order to clarify whether the origin of the anisotropy in the electrical conductivity is difference in the carrier effective mass or not, we performed X-ray absorption spectroscopy (XAS). The O K-edge spectra of WO$_{2.853}$ collected photon energy from 525 to 560 eV with linearly-polarized beams (**Figure 5a**). The beam along the tunnel is $E_{//}$ and the beam across the tunnel is $E_\perp$. In **Figure 5b**, the peak A and B refer O 2p$-$W 5d t$_{2g}$ hybridization, C and

D refer O 2p−W 5d e_g hybridization, and E and F refer O 2p−W 6sp hybridization, respectively.[20-22] There is no significant difference between the XAS spectra across and along the tunnel, indicating that the anisotropy in the electronic structure is small most likely due to widely spread W 5d orbital. Since there is no significant difference in the peak A and B, the anisotropy in the carrier effective mass is negligibly small. From these results, we concluded that the anisotropy in the electrical conductivity of the 1D atomic defect tunnels are originated by the anisotropy of the relaxation time. Simply, the 1D atomic defect tunnels scatter carrier electrons.

CONCLUSIONS

In this study, we focused on the anisotropy in the electrical conductivity of simple transition metal oxide (TMO), oxygen-deficient WO_x with the anisotropic crystal structure. We fabricated several WO_x films by pulsed laser deposition technique on lattice matched $LaAlO_3$ substrate under controlled oxygen atmosphere. The crystallographic analyses of the WO_x films revealed that highly dense atomic defect tunnels were aligned one dimensionally along [100] $LaAlO_3$. The electrical conductivity (σ) along the 1D atomic defect tunnels was ~5 times larger than that across the tunnels; When $x = 2.778$, the σ along [001] was 1700 S cm^{-1} whereas that along [1$\bar{1}$0] was 360 S cm^{-1}. The origin of this anisotropy of σ is the difference in the crystal structure between along [001] and along [1$\bar{1}$0], which are originated from the formation of the 1D atomic defect tunnels. The present approach, introduction of 1D atomic

defect tunnels might be useful to design simple TMOs exhibiting anisotropic electrical conductivity.

EXPERIMENTAL SECTION

Fabrication and analyses of oxygen-deficient WO$_x$ epitaxial films. Oxygen-deficient WO$_x$ epitaxial films were heteroepitaxially grown on lattice-matched (110) LaAlO$_3$ substrate by pulsed laser deposition (PLD) technique at a substrate temperature of 600 °C under controlled oxygen atmosphere (4.0 – 8.3 Pa). The fluence of the KrF excimer laser and repetition rate were set to ~1 J cm^{-2} pulse^{-1} and 10 Hz, respectively. The typical growth rate was ~15 pm pulse^{-1}.

After the film growth, we obtained high-energy electron diffraction (RHEED) patterns before exposure to air. Then, we took out and analyzed the films. The film thickness was measured by X-ray reflectivity (XRR) using monochromated Cu Kα$_1$ radiation (ATX-G, Rigaku Co.). The thickness was ~45 nm in all cases. The valence states of W ion in the WO$_x$ films were analyzed by X-ray photoelectron spectroscopy (XPS) using Al Kα radiation (1486.6 eV). We evaluated the ratio of W^{4+}, W^{5+}, and W^{6+} using the W 4f (30−40 eV) core-level spectra. The lattice parameters of the WO$_x$ were analyzed by high-resolution X-ray diffraction (XRD) using monochromated Cu Kα$_1$ radiation. Out-of-plane and in-plane Bragg diffraction patterns were measured. The film surface was observed by an atomic force microscopy (AFM, MFP-3D Origin, Oxford Instruments Co.). The atomic arrangement around the film and the substrate interface was visualized using scanning transmission electron microscopy (STEM,

JEM-ARM200CF, JEOL Co. Ltd) operated at 200 keV. High-angle annular dark-field (HAADF) images were taken with detection angle of 68 – 280 mrad.

Electron transport properties. The electrical conductivity (σ) of the resultant WO_x films was measured along [100] and [1$\bar{1}$0] $LaAlO_3$ substrate by dc four-probe method with four equally-spaced, co-linear probes at a temperature ranging 30 – 300 K. In-Ga alloy was used as the contact electrodes. Thermopower (S) was measured by a steady- state method at room temperature. The detail of our S measurement has been described elsewhere.[23]

The electronic structure. X-ray absorption spectroscopy (XAS) measurements using two orthogonal linearly-polarized beams were performed at the 2A beamline Pohang accelerator laboratory (PAL). An energy resolution is ~0.1 eV. Total electron yield (TEY) was monitored. Two linearly-polarized X-ray beams, normal to film surface, were used to see the difference in x-ray absorption along two in-plane direction ($E_{//}$ [001] WO_x and $E_{\perp}$ [001] WO_x). The XAS O K-edge spectrum was measured from 525 to 560 eV at room temperature.

ASSOCIATED CONTENT

Supporting Information

The Supporting Information is available free of charge at DOI

Anisotropy in electrical conductivity of transition metal oxide; X-ray photoelectron spectroscopy; Temperature dependent electrical conductivity;

AUTHOR INFORMATION

Corresponding authors

Gowoon Kim − Graduate School of Information Science and Technology, Hokkaido University, N14W9, Kita, Sapporo 060−0814, Japan;

ORCiD: orcid.org/0000-0002-5803-839X; E-mail: woom93@gmail.com

Hiromichi Ohta − Graduate School of Information Science and Technology, Hokkaido University, N14W9, Kita, Sapporo 060−0814, Japan; Research Institute for Electronic Science, Hokkaido University, N20W10, Kita, Sapporo 001−0020, Japan;

ORCiD: orcid.org/0000-0001-7013-0343; E-mail: hiromichi.ohta@es.hokudai.ac.jp

Authors

Bin Feng − Institute of Engineering Innovation, The University of Tokyo, 2−11−16 Yayoi, Bunkyo, Tokyo 113−8656, Japan;

ORCiD: orcid.org/0000-0002-4306-2979

Sangkyun Ryu − Department of Physics, Pusan National University, Busan 46241, South Korea;

ORCiD: orcid.org/0000-0003-4817-538X

Hai Jun Cho − Graduate School of Information Science and Technology, Hokkaido University, N14W9, Kita, Sapporo 060−0814, Japan; Research Institute for Electronic Science, Hokkaido University, N20W10, Kita, Sapporo 001−0020, Japan;

ORCiD: orcid.org/0000-0002-8642-4183

Hyoungjeen Jeen − Department of Physics, Pusan National University, Busan 46241, South Korea;

ORCiD: orcid.org/0000-0003-2922-377X

Yuichi Ikuhara − Institute of Engineering Innovation, The University of Tokyo, 2−11−16 Yayoi, Bunkyo, Tokyo 113−8656, Japan;

ORCiD: orcid.org/0000-0003-3886-005X

Author contributions

G.K. performed the sample preparation and measurements. B.F. and Y.I. performed the STEM analyses. S. R and H. J. performed the XAS analyses. H.J.C. performed XPS analyses. G.K. and H.O. planned and supervised the project. All authors discussed the results and commented on the manuscript.

Notes

The authors declare no competing financial interest.

REFERENCES

(1) Liu, E.; Fu, Y.; Wang, Y.; Feng, Y.; Liu, H.; Wan, X.; Zhou, W.; Wang, B.; Shao, L.; Ho, C.-H. Integrated Digital Inverters Based on Two-Dimensional Anisotropic ReS_2 Field-Effect Transistors. *Nat. Commun.* **2015,** *6*, 1-7.

(2) Afsari, S.; Yasini, P.; Peng, H.; Perdew, J. P.; Borguet, E. Anisotropic Conductivity at the Single-Molecule Scale. *Angew. Chem. Int. Ed.* **2019,** *58*, 14275-14280.

(3) Wang, H.; Chen, M.-L.; Zhu, M.; Wang, Y.; Dong, B.; Sun, X.; Zhang, X.; Cao, S.; Li, X.; Huang, J. Gate Tunable Giant Anisotropic Resistance in Ultra-Thin GaTe. *Nat. Commun.* **2019,** *10*, 1-8.

(4) Funahashi, M. Anisotropic Electrical Conductivity of n-doped Thin Films of Polymerizable Liquid-Crystalline Perylene Bisimide Bearing a Triethylene Oxide Chain and Cyclotetrasiloxane Rings. *Mater. Chem. Front* **2017,** *1*, 1137-1146.

(5) Gong, S.; Zhu, Z.; Meguid, S. Anisotropic Electrical Conductivity of Polymer Composites with Aligned Carbon Nanotubes. *Polym.* **2015,** *56*, 498-506.

(6) Zhao, S.; Dong, B.; Wang, H.; Wang, H.; Zhang, Y.; Han, Z. V.; Zhang, H. In-plane Anisotropic Electronics Based on Low-symmetry 2D Materials: Progress and Prospects. *Nanoscale Adv.* **2020,** *2*, 109-139.

(7) Zhao, L.-D.; Lo, S.-H.; Zhang, Y.; Sun, H.; Tan, G.; Uher, C.; Wolverton, C.; Dravid, V. P.; Kanatzidis, M. G. Ultralow Thermal Conductivity and High Thermoelectric Figure of Merit in SnSe Crystals. *Nature* **2014,** *508*, 373-377.

(8) Shen, C.; Calderon, J. E.; Barrios, E.; Soliman, M.; Khater, A.; Jeyaranjan, A.; Tetard, L.; Gordon, A.; Seal, S.; Zhai, L. Anisotropic Electrical Conductivity in Polymer Derived Ceramics Induced by Graphene Aerogels. *J. Mater. Chem. C* **2017,** *5*, 11708-11716.

(9) Zhuang, Y.; Zheng, K.; Cao, X.; Fan, Q.; Ye, G.; Lu, J.; Zhang, J.; Ma, Y. Flexible Graphene Nanocomposites with Simultaneous Highly Anisotropic Thermal and Electrical Conductivities Prepared by Engineered Graphene with Flat Morphology. *ACS nano* **2020,** *14*, 11733-11742.

(10) Kuntscher, C.; Schuppler, S.; Haas, P.; Gorshunov, B.; Dressel, M.; Grioni, M.; Lichtenberg, F.; Herrnberger, A.; Mayr, F.; Mannhart, J. Extremely Small Energy Gap in the Quasi-One-Dimensional Conducting Chain Compound $SrNbO_{3.41}$. *Phys. Rev. Lett.* **2002,** *89*, 236403.

(11) Pautrat, A.; Kobayashi, W. Dominant Role of Impurity Scattering over Crystalline Anisotropy for Magnetotransport Properties in the Quasi-One-Dimensional Hollandite $Ba_{1.2}Rh_8O_{16}$. *Phys. Rev. B* **2010,** *82*, 115113.

(12) Huangfu, S.; Jakub, G. D.; Zhang, X.; Blacque, O.; Puphal, P.; Pomjakushina, E.; von Rohr, F. O.; Schilling, A. Anisotropic Character of the Metal-to-Metal Transition in $Pr_4Ni_3O_{10}$. *Phys. Rev. B* **2020,** *101*, 104104.

(13) Yamaura, K.; Arai, M.; Sato, A.; Karki, A.; Young, D.; Movshovich, R.; Okamoto, S.; Mandrus, D.; Takayama-Muromachi, E. NaV_2O_4: a Quasi-1D Metallic Antiferromagnet with Half-Metallic Chains. *Phys. Rev. Lett.* **2007,** *99*, 196601.

(14) Greenblatt, M. Molybdenum Oxide Bronzes with Quasi-Low-Dimensional Properties. *Chem. Rev.* **1988,** *88*, 31-53.

(15) Ando, Y.; Segawa, K.; Komiya, S.; Lavrov, A. Electrical Resistivity Anisotropy from Self-Organized One Dimensionality in High-Temperature Superconductors. *Phys. Rev. Lett.* **2002,** *88*, 137005.

(16) Mao, Z.; He, T.; Rosario, M.; Nelson, K.; Okuno, D.; Ueland, B.; Deac, I.; Schiffer, P.; Liu, Y.; Cava, R. Quantum Phase Transition in Quasi-One-Dimensional $BaRu_6O_{12}$. *Phys. Rev. Lett.* **2003,** *90*, 186601.

(17) Kim, G.; Zhang, Y. Q.; Min, T.; Suh, H.; Jang, J. H.; Kong, H.; Lee, J.; Lee, J.; Jeon, T. Y.; Lee, I. Extremely Light Carrier-Effective Mass in a Distorted Simple Metal Oxide. *Adv. Electron. Mater.* **2018,** 1800504.

(18) Pickering, R.; Tilley, R. An Electron Microscope Study of Tungsten Oxides in the Composition Range $WO_{2.90}$-$WO_{2.72}$. *J. Solid State Chem.* **1976,** *16*, 247-255.

(19) Kim, G.; Feng, B.; Sheu, Y.-M.; Cho, H. J.; Ikuhara, Y.; Ohta, H. Coexistence of High Electron Conduction and Low Heat Conduction in Tungsten Oxide Epitaxial Films with 1D Atomic Defect Tunnels. *ACS Appl. Electron. Mater.* **2020,** *2*, 2507-2513.

(20) Purans, J.; Kuzmin, A.; Parent, P.; Laffon, C. X-ray Absorption Study of the Electronic Structure of Tungsten and Molybdenum Oxides on the O K-edge. *Electrochim. Acta* **2001,** *46*, 1973-1976.

(21) Purans, J.; Kuzmin, A.; Parent, P.; Laffone, C. Study of the Electronic Structure of Rhenium and Tungsten Oxides on the O K-edge. *Ionics* **1998,** *4*, 101-105.

(22) Chen, B.; Laverock, J.; Piper, L.; Preston, A.; Cho, S.; DeMasi, A.; Smith, K.; Scanlon, D.; Watson, G.; Egdell, R. The Band Structure of WO_3 and Non-Rigid-Band Behaviour in $Na_{0.67}WO_3$ Derived from Soft X-ray Spectroscopy and Density Functional Theory. *J. Phys.: Condens. Matter* **2013,** *25*, 165501.

(23) Ohta, H.; Kim, S.; Mune, Y.; Mizoguchi, T.; Nomura, K.; Ohta, S.; Nomura, T.; Nakanishi, Y.; Ikuhara, Y.; Hirano, M. Giant Thermoelectric Seebeck Coefficient of a Two-Dimensional Electron Gas in $SrTiO_3$. *Nat. Mater.* **2007,** *6*, 129-134.
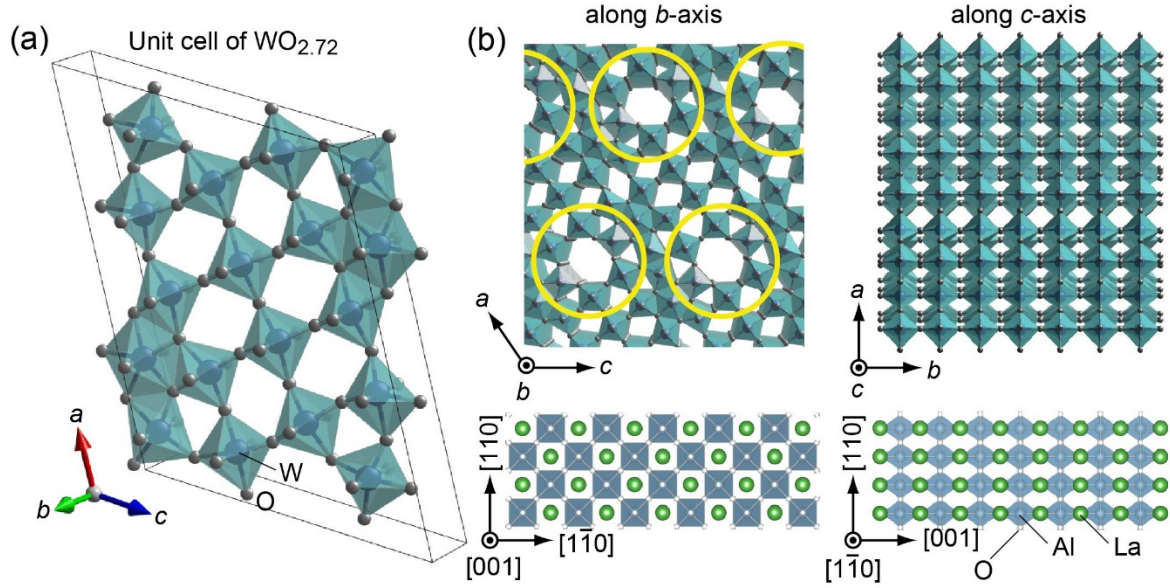
Figure 1. (a) Schematic crystal structure of $WO_{2.72}$. (b) Side (or cross-sectional) views based on assumed film growth of oxygen deficient WO_x on (110) oriented $LaAlO_3$ substrate. Almost no similarity of the atomic arrangement between WO_x along b-axis and $LaAlO_3$ along [001]. On the other hand, the distance between two neighboring oxygens in WO_x along c-axis and $LaAlO_3$ along [1$\bar{1}$0] is same (0.379 nm). We expected the atomic defects (yellow ring) are aligned along [001], making 1D atomic defect tunnels.
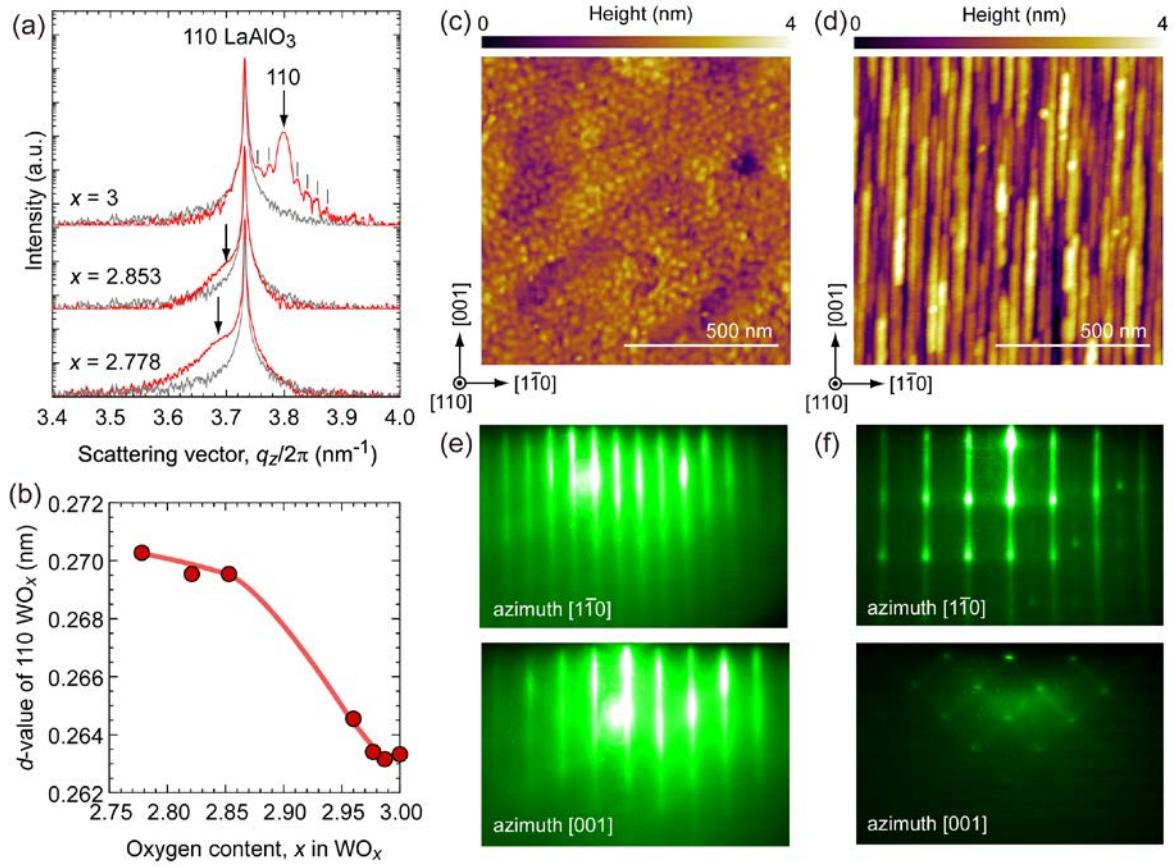
Figure 2. Structural analyses. (a) Out-of-plane XRD patterns of the WO_x films around 110 $LaAlO_3$. The gray dashed line indicates bare $LaAlO_3$ substrate. The diffraction peak position of WO_x is indicated with arrow ($\downarrow$). (b) Change in the d-value of 110 WO_x. The d-value increases with decreasing x. Topographic AFM images of (c) WO_3 and (d) $WO_{2.778}$ epitaxial films. Structural anisotropy is clearly visualized in (d). RHEED patterns of (e) WO_3 and (f) $WO_{2.778}$ epitaxial films. The directions on AFM images and RHEEED patterns are direction of $LaAlO_3$ substrate.
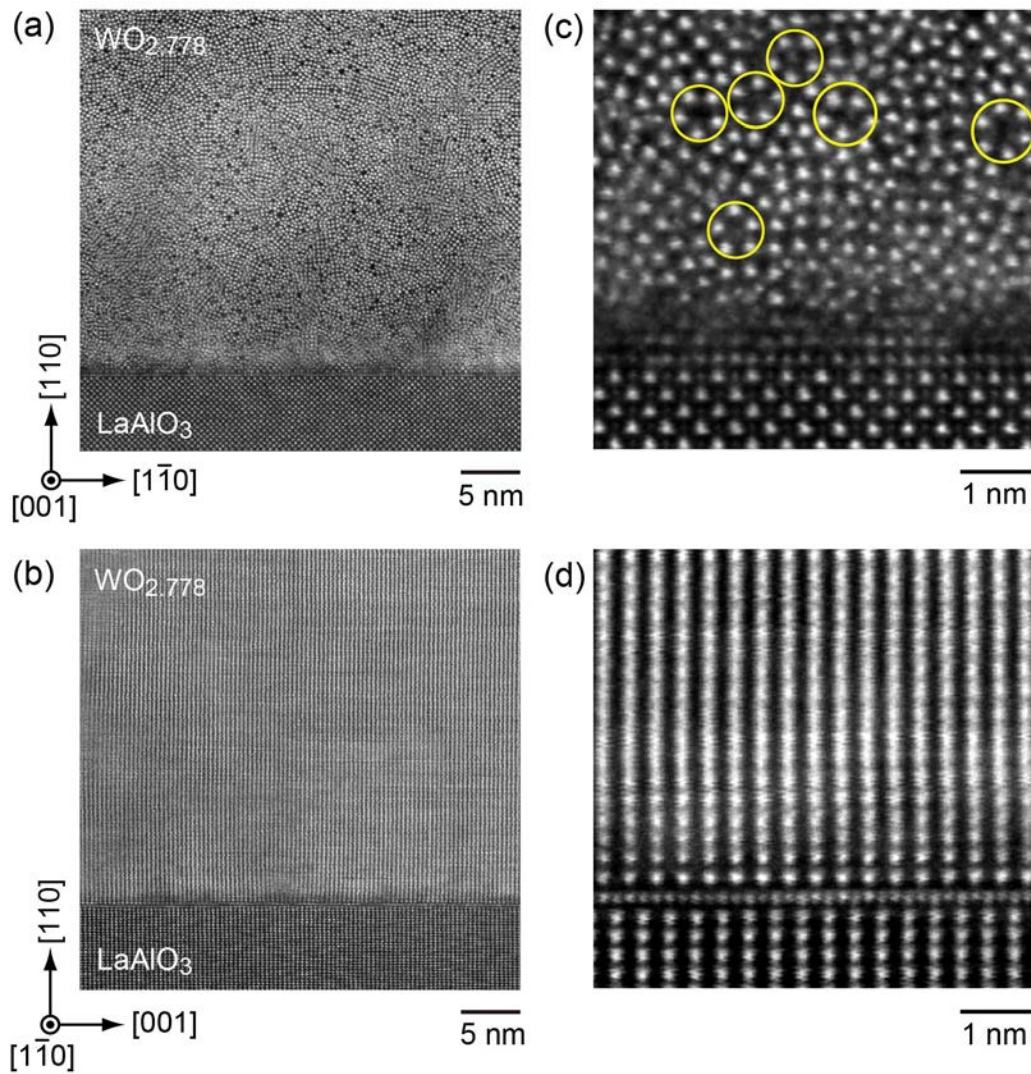
Figure 3. Visualization of 1D atomic defect tunnels. Cross-sectional HAADF-STEM images of the WO$_{2.778}$ film along (a) [001] and (b) [1$\bar{1}$0]. The scale bar is 5 nm. Highly dense atomic defect tunnels are clearly visualized along [001], whereas only square lattices are seen along [1$\bar{1}$0].
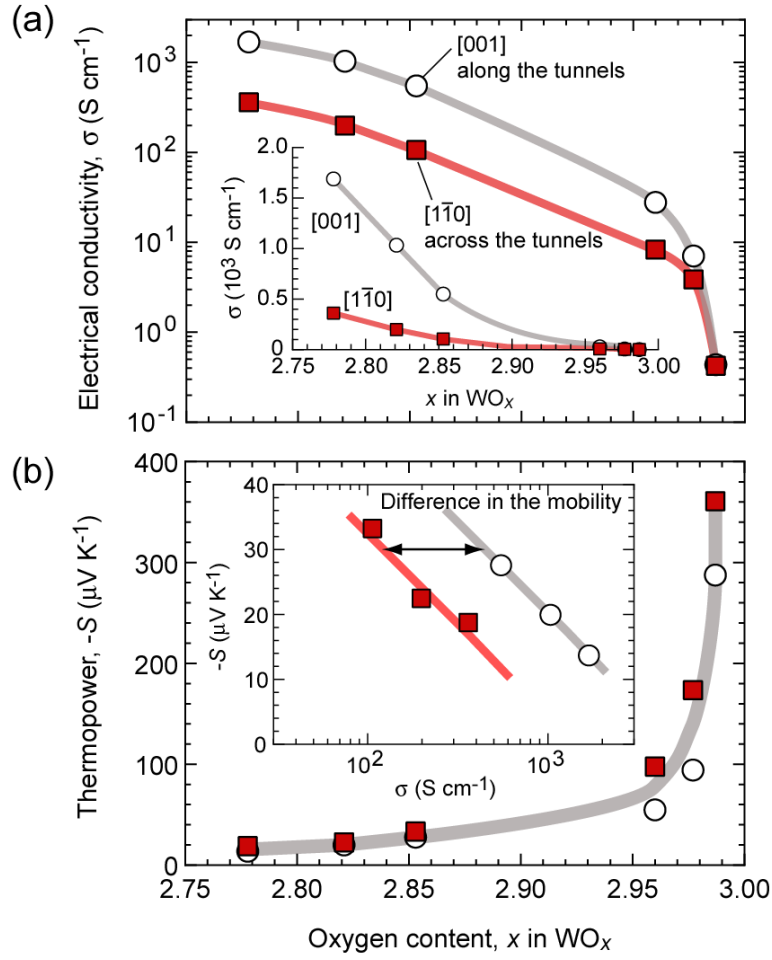
Figure 4. (a) Electrical conductivity (σ) and (b) thermopower (S) of the WO$_x$ films along [001] and [1$\bar{1}$0] at room temperature. (Inset in a) Linear scaled. (Inset in b) Jonker plot of x = 2.778, 2.82 and 2.853. When $x < 2.98$, anisotropy of the σ is obviously observed whereas such anisotropy of the S is not observed. The Jonker plot clearly indicates that the mobility along [001] is higher than that along [1$\bar{1}$0].
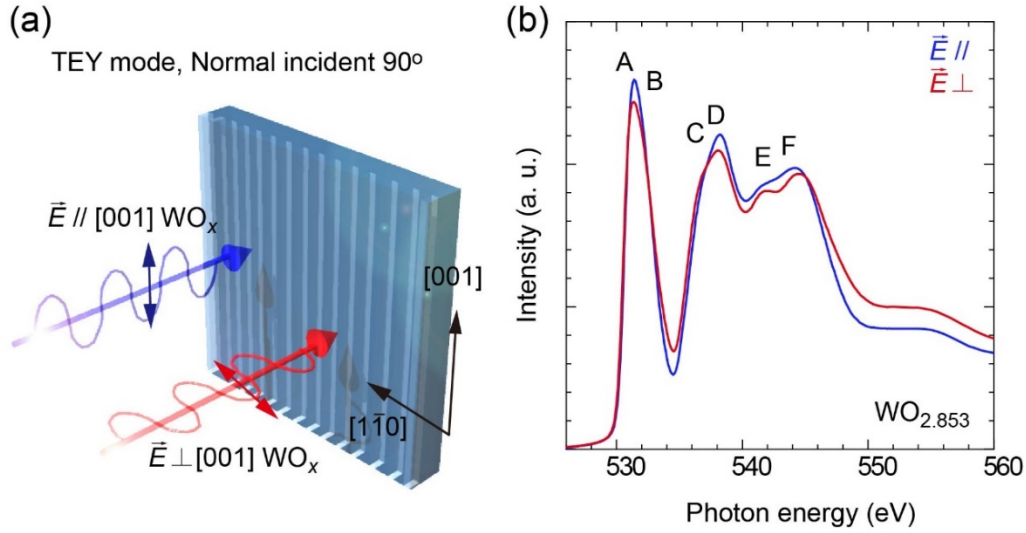
Figure 5. O K-edge spectra measured by X-ray absorption spectroscopy with total electron yield (TEY) mode. (a) The linearly polarized beam incidence along the tunnel ($E_{//}$) and across the tunnel ($E_{\perp}$). (b) The peak A and B refer O 2p–W 5d t_{2g} hybridization, C and D refer O 2p–W 5d e_g hybridization, and E and F refer O 2p–W 6sp hybridization, respectively. There is no significant difference in the peak A and B, indicating that the anisotropy in the carrier effective mass is negligibly small.

Table of content

Anisotropy in the Electrical Conductivity of Simple Transition Metal Oxide

Lower electrical conductivity

Higher electrical conductivity